A Silatrane:Molecule-Based Crystal Composite Solid-State Electrolyte for All-Solid-State Lithium Batteries

Adriana M. Navarro-Suárez*[a] and Patrik Johansson[a, b]

All-solid-state batteries (ASSBs) are promoted as a promising option towards higher energies and power densities as well as drastically reduced safety risks as compared to conventional lithium-ion batteries (LIBs). Herein, a composite solid-state electrolyte (SSE) based on two crystalline materials with two distinctly different ion conduction mechanisms, percolation and ion hopping, is reported. By combining a silatrane (SA; here ethoxysilatrane) with a molecule-based crystal (MBC; here LiTFSI-TMEDA) the resulting SA:MBC 2:1 crystalline composite shows an appreciable ion conductivity of 10^{-5} S cm^{-1} at room temperature, and low apparent activation energy, 836 K, for the ion transport. Studies of the overall and local structure show that in the composite the Li$^+$ and TFSI ions are dissociated, and this seems to be mediated by the SA part of the matrix. As a proof-of-concept, an ASSB based on this SSE can operate at 50 °C providing up to 105 mAh g^{-1} during 20 cycles.

1. Introduction

All solid-state batteries (ASSBs) are promoted as a promising option, not only for higher energy and power densities as compared to conventional lithium-ion batteries (LIBs) – but also due to their electrochemical and thermal stabilities, high ion selectivity and reduced safety risks – primarily by avoiding any flammable organic electrolyte solvents.[1,2] A wide variety of solid-state electrolytes (SSEs) for Li batteries have been developed, ranging from inorganic ceramic electrolytes to solid polymer electrolytes.[3] However, in order to satisfy practical applications it is necessary to design SSEs with structure and dynamics improving the ion conductivity and interfacial properties as well as simplifying the preparation process.[1,4]

In crystalline solid materials, fast ion transport generally relies on the concentration and distribution of defects, i.e. via an ion hopping mechanism.[1] Some materials, however, can achieve high ion conductivities without any high concentration of defects, but rather being composed of two sub-lattices; one crystalline framework of immobile ions and one of mobile ions/species. The diffusion pathway for the mobile ions is then dependent on the percolation network.[5]

Some molecule-based crystals (MBCs) show selective lithium ion conduction,[6–9] based on an ion hopping mechanism attributed to repeated formation and breaking of electrostatic interactions between the moving lithium ions and the atoms of the host lattice – often in channel-like paths.[8]

Molecules with large internal dipole moments, such as silatranes (SAs), have been used as matrices for a wide range of lithium salts: lithium triflate (LiOTf), lithium bis(trifluoromethanesulfonyl) imide (LiTFSI), lithium hexafluorophosphate (LiPF$_6$), and lithium bis(oxalato)borate (LiBOB), to create electrolytes conducting lithium ions via percolation networks.[10,11] A silatrane, with the general formula $C_6H_{12}NO_3Si–Z$, where Z is the axial substituent, can be seen as a cage created of three heterocyclic rings sharing two transannular atoms, a silicon atom and a nitrogen atom, with the lone electron pair of the latter acting as an electron-donor to the former. This has several consequences: the SA becomes very stable vs. interaction with external reactants, and the silicon atom can be considered pentacoordinated and thus hypervalent. The ion conductivity resulting when using SA matrices depends both on the length of the transannular Si–N dative bond and on the axial substituent.[12]

Here we have created an ion conducting material, based on paths for both ion hopping and percolation, by combining an SA of ethoxysilatrane (Figure 1a) and an MBC of LiTFSI and tetramethylethylenediamine (TMEDA) (Figure 1b) with ordered arrays of channels containing the lithium ions. The ion

[a] Dr. A. M. Navarro-Suárez, Prof. P. Johansson
    Department of Physics
    Chalmers University of Technology
    412 96 Gothenburg (Sweden)
    E-mail: adriana.navarrosuarez@chalmers.se
[b] Prof. P. Johansson
    ALISTORE – European Research Institute
    CNRS FR 3104, Hub de l'Energie
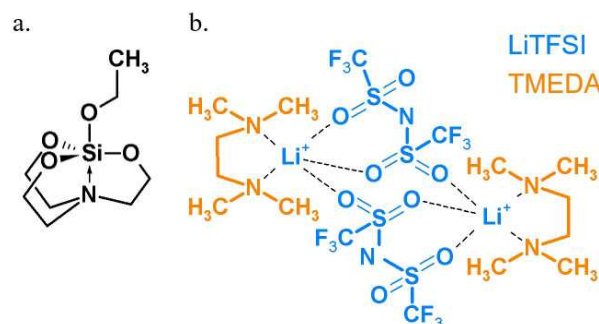   15 Rue Baudelocque
    80039 Amiens (France)

Figure 1. Molecular structures of (a) SA, and (b) MBC.

conductivities of composites with different ratios SA:MBC and content/doping of LiTFSI were studied and an SA:MBC 2:1 composite was selected for more in depth studies due to its high ion conductivity. We primarily address the very fundamentals such as overall and local structure as well as thermal stability of this material, but we also assess it as an SSE operated in a proof-of-concept ASSB.

2. Results and Discussion

We start by selecting the best SSE composition based on the ion conductivity, and by comparing the VFT and Arrhenius fits, using both the composite and the constituents, we also propose an ion conduction mechanism. The overall and local structures are then unveiled together with the thermal stabilities whereafter the electrochemistry is assessed including usage of an SSE in a proof-of-concept ASSB.

2.1. Ion Conductivities

By assessing the ion conductivity for all the LiTFSI/SA complexes synthesized (Figure S1), it is clear that linear alkane-substituted SAs favour higher ion conductivities and therefore ethoxysilatrane was selected as the SA component. By varying the ratio of the components a ratio of 2:1 SA:MBC was finally selected for further studies as it presented the highest ion conductivity in the whole temperature range (Figure S2a).

At high frequency the Nyquist plot of LiTFSI/SA, MBC and SA:MBC 2:1 (Figure 2a–c) exhibit single semi-circles and hence
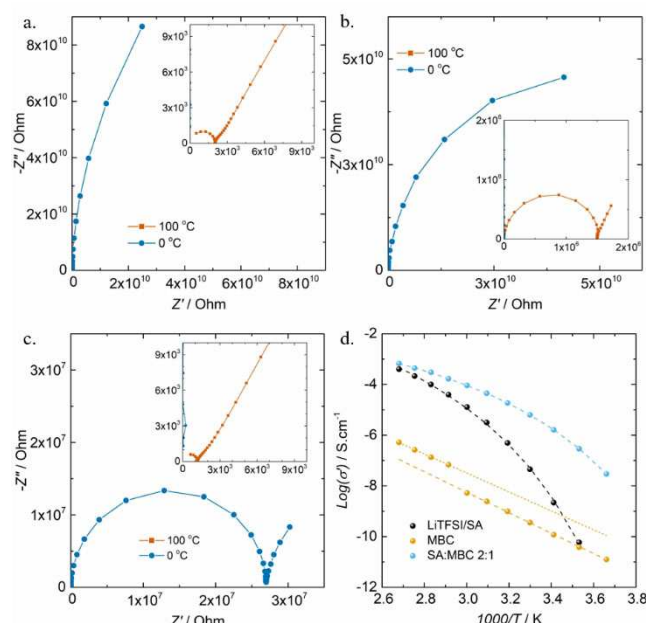
the ion conductivities cannot be separated into bulk and grain boundary contributions for neither of the three materials.

The ion conductivities for LiTFSI/SA and MBC have previously been reported to be 120 and 80 $\mu S\,cm^{-1}$ at 60 °C, respectively.[10,13] We obtain roughly a magnitude lower conductivities; 12.8 and 0.4 $\mu S\,cm^{-1}$, respectively (Figure 2d and Figure S3). This is likely due to differences in sample preparation, *e.g.* drying procedure and/or thickness of the samples, measurement method *i.e.* broadband dielectric spectroscopy *vs.* a more limited frequency range, and/or levels of impurities. Notably, with respect to the former, in the previous studies no Karl Fischer titrations are reported and hence the water contents are not known. The kink in the Arrhenius fit to the ion conductivity of MBC between 60 to 70 °C correlates well with the phase transition observed at 81 °C by DSC (see Figure 4c).[14] As the combination of SA and MBC creating the composite increases the ion conductivity, the transannular dative bond of the SA is inferred to dissociate the LiTFSI salt and induce a large number of charge carriers,[10] while MBC provides the lithium ions created with conduction paths.[13]

The conductivity data were fitted to a VFT for LiTFSI/SA and SA:MBC 2:1 and the Arrhenius equation for MBC (Table 1). For

Table 1. Fitting parameters used in Figure 2.

Material	σ_0 [$S\,cm^{-1}$]	B [K]	T_0 [K]
LiTFSI/SA	$(4.68 \pm 0.09) \times 10^{-1}$	$(8.56 \pm 0.20) \times 10^2$	$(2.52 \pm 0.01) \times 10^2$
MBC (T $\leq$ 60 °C)	$(8.04 \pm 0.05) \times 10^2$	$(8.58 \pm 0.18) \times 10^3$	–
MBC (T $>$ 60 °C)	$(1.04 \pm 0.01) \times 10^3$	$(8.85 \pm 0.16) \times 10^3$	–
SA:MBC 2:1	$(1.64 \pm 0.05) \times 10^{-1}$	$(8.36 \pm 0.23) \times 10^2$	$(2.21 \pm 0.20) \times 10^2$

the MBC, we used two separate Arrhenius fittings, one before the phase transition (0– $\leq$ 60 °C) and another after ($>$ 60– 100 °C).

Fitting parameter σ_0 is explicitly a conductivity at infinite temperature, related directly to the number of ions, and the attempt frequency for ions to transition between solvation sites, while B, the apparent activation energy, is related to the energy of the transition state involved.[15] The high σ_0 for MBC, before and after the phase transition, is not surprising given that lithium and TFSI ions are parts of the framework, while the high apparent activation energy is likely caused by strong Li–O interactions.[9] Nevertheless, the phase transition has been related to anion disordering,[14] as also observed for other crystalline compounds.[16,17] The Arrhenius dependence points towards a conductivity mainly related to diffusion of Li^+ ions, possibly assisted by the anion disorder. LiTFSI/SA has a lower σ_0, consistent with a percolation mechanism, but the lower B still allows for a higher ion conductivity than that of MBC. The SA:MBC 2:1 composite has the lowest σ_0, and would thus have the lowest ion conductivity at infinite temperature, but in practice shows the highest ion conductivity due to its low apparent activation energy.

Figure 2. AC impedance Nyquist plot at 0 and 100 °C of (a) LiTFSI/SA, (b) MBC and (c) SA:MBC 2:1. (d) Arrhenius plot for the three materials. Dashed lines correspond to their respective fittings.

Articles

Increasing the concentration of charge carriers by adding up to 15 mol% extra of LiTFSI to the SA:MBC 2:1 composite result in a slight increase in the conductivity across the entire temperature range (Figure S2b). However, when the amount of LiTFSI was further increased, the conductivity decreased, probably because of increased ion-pairing/salt aggregation. Focus is henceforth on SA:MBC 2:1, to avoid complicating effects caused by any extra LiTFSI.

2.2. Structural Characterization

The overall and local structural differences between SA, MBC and SA:MBC 2:1 were analysed by XRD, FTIR and Raman (Figure 3). We know of no XRD reports for pure SA, but it is
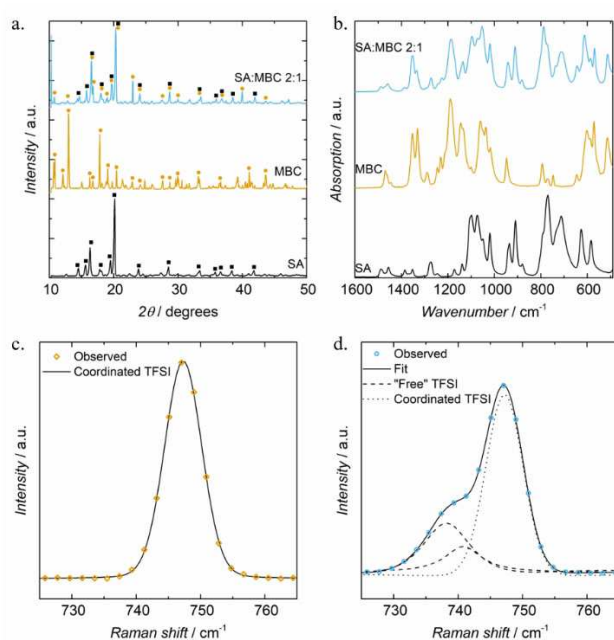
Figure 3. (a) X-ray diffractograms and (b) Fourier-transform infrared spectra of SA, MBC, and SA:MBC 2:1. Deconvoluted Raman spectra of (c) MBC and (d) SA:MBC 2:1. LiTFSI is partially dissociated in the SA:MBC 2:1 composite.

clear that reflections corresponding to both SA and MBC are observable in SA:MBC 2:1 (Figure 3a). The intensities of the MBC reflections are small, in agreement with the lower content of MBC in the composite. The presence of MBC seems to cause a lattice strain in the SA, seen as a shift in the SA:MBC 2:1 reflections towards higher angles, i.e. shorter interlayer distances, as compared to pure SA.

The local structures in the SA, the MBC crystals and their 2:1 composite were further analysed by FTIR and Raman spectroscopy (Figure 3b–d). The FTIR spectrum of SA has previously been reported by Voronkov[18] and we here provide tentative assignments of both the MBC and SA:MBC 2:1 spectra based on the assignments of Rey *et al.,*[19] Sanders *et al.,*[20] and Wen *et al.*[21] (Table S1). To assess the local structure changes from separate components to the composite,

we generated an artificial spectrum by multiplying the SA spectrum by 2 and adding the MBC spectrum (Figure S4). By comparing this with the experimental spectrum of SA:MBC 2:1, the 860–1030 cm^{-1} region was found suitable for normalization for assessing differences between the spectra. The peaks at 1352, 1225, 1187, 1052, 612, and 512 cm^{-1} all increase and all of them are stretching and bending modes of TFSI in the MBC structure. In contrast, the peaks with decreasing intensities; at 585, 714, 1072, 1136 and 1458 cm^{-1}, are all stretching and bending modes of SA. The peak at 769 cm^{-1} in SA is shifted to 787 cm^{-1} in SA:MBC 2:1, indicating a weakened interaction between Si and O.[22] The small peak at 746 cm^{-1} in the artificial spectrum, from Li and TFSI ion-ion interaction, appear as a shoulder at 740 cm^{-1} in the experimental spectrum, implying that in the composite there is rather "free" TFSI.[23−25] Furthermore, this region of the TFSI anion vibrational spectrum has also been extensively studied by Raman spectroscopy.[26−28] Here the SA does not present any Raman bands in this region (not shown), while MBC has a peak at 747 cm^{-1} (Figure 3c), due to ion-pair formation,[29,30] and as it can be well fitted by using only one pseudo-Voigt function this indicates that all the TFSI anions are coordinated by Li. In the composite, a shoulder appears at 739 cm^{-1} (Figure 3d), which likely is due to the SA dissociating the ion-pairs and creating "free" TFSI anions, and by a fit using 3 pseudo-Voigt functions ("free" TFSI in both transoid and cisoid conformers)[30,31] we find that ∼38±3.7% of the TFSI anions are "free", in agreement with the higher ion conductivity. Thus both the long range and local structure, probed by XRD, and FTIR and Raman, respectively, show that in the composite the SA is responsible for dissociating the LiTFSI salt, causing a lattice strain in the SA. It has previously been observed that the presence of "free" TFSI anions and the lattice strain in MBCs indicate selective lithium conduction as some of the lithium ions secure the channel structure suppressing anion conduction.[6]

2.3. Thermal Stability and Phase Transitions

Starting with the TGA traces, these show that SA decomposes above 160 °C, while the decomposition of MBC begins at ∼110 °C, and that the mass remaining at the plateau at ∼300–350 °C, also for the composite, roughly corresponds to the LiTFSI content (Figure 4a). This indicates that the thermal decomposition occurs in two stages for the MBC and the composite; a gradual mass loss from 110 to 295 °C which most likely is due to evaporation of TMEDA out of the MBC, and then a more distinct second mass loss with an approximate onset temperature of 370 °C, which can be assigned to the thermal degradation of LiTFSI. For SA:MBC 2:1 there is almost no weight loss up to 180 °C, i.e. some hysteresis as compared with pure MBC, indicating interactions between MBC and SA making the processes more sluggish.

Turning to the DSC traces SA exhibited a single endothermal peak at 97.7 °C corresponding to the melting temperature and with a heat of fusion (ΔH°_{fus}) of 44.2 J g^{-1} (Figure 4b). On cooling, SA crystallized with an exothermic peak at 69.4 °C
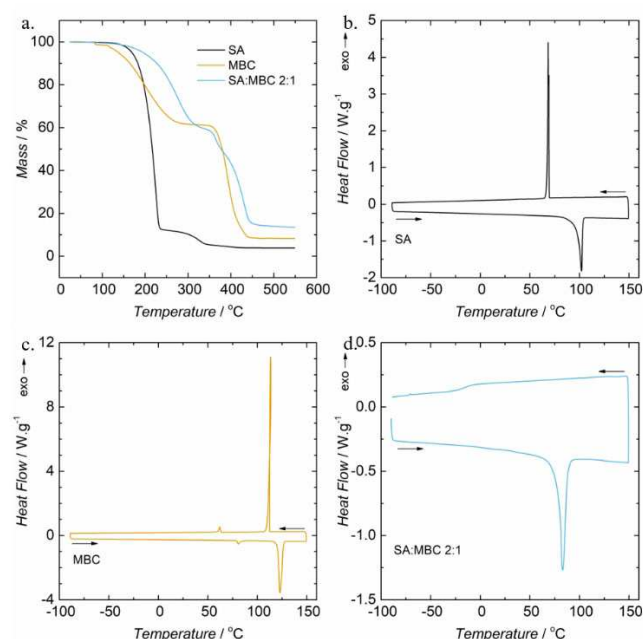
Figure 4. (a) TGA and (b–d) DSC of SA, MBC, and SA:MBC 2:1.

Figure 5. LSV for the SA:MBC 2:1 composite. WE: Ni foil. RE and CE: Li foil. Scan rate: 1 mV s^{-1}.

($\Delta H^{\circ}_{fus} = 36.1$ J g^{-1}). MBC presented a small solid-solid transition at 81 °C before melting at 120.8 °C ($\Delta H^{\circ}_{fus} = 75.9$ J g^{-1}) and upon cooling crystallized at 112.4 °C ($\Delta H^{\circ}_{fus} = 75.9$ J g^{-1}) and an exothermic transition at 62 °C, likely again a solid-solid transition (Figure 4c). The kink on the MBC Arrhenius plot (Figure 2d) occurs at lower temperatures than the solid-solid transition, likely due to the sensitivity of MBC to the heating rate, which is different in the dielectric instrument as compared to the DSC. For SA:MBC 2:1, on the first heating from −90 °C, there was one endothermic phase transition at 70 °C (melting) with a ΔH°_{fus} of 45.2 J g^{-1}. The lack of a step in the Arrhenius plot (Figure 2d) indicates that the ion conductivity in the solid state is relatively high for this composite. When the temperature was decreased the sample solidified from the melt to a glassy amorphous state at −16.0 °C. This is not caused by a too fast cooling rate as this behaviour was observed at different scan rates (Figure S5). Instead, we suspect that SA:MBC 2:1 might be a metastable crystal that crystallizes only in the presence of certain solvents.[32] T_0 has been reported to be approximately 40 °C below the glass transition temperature (T_g),[33] here T_0 (Table 1) is 35 °C lower than the T_g (Figure 4d).

2.4. Electrochemistry and Battery Tests

LSV was performed on SA:MBC 2:1 to assess the ESW, showing it to be electrochemically stable between −0.1 and 3.6 V *vs.* Li$^+$/Li, hence an overall ESW of ~3.7 V (Figure 5). The anodic stability limit is most probably determined by the methyl group of TMEDA, while the cathodic stability limit corresponds to lithium deposition.[34] The set of minor reduction peaks starting at 1.4 V are most likely related to SEI formation on the nickel

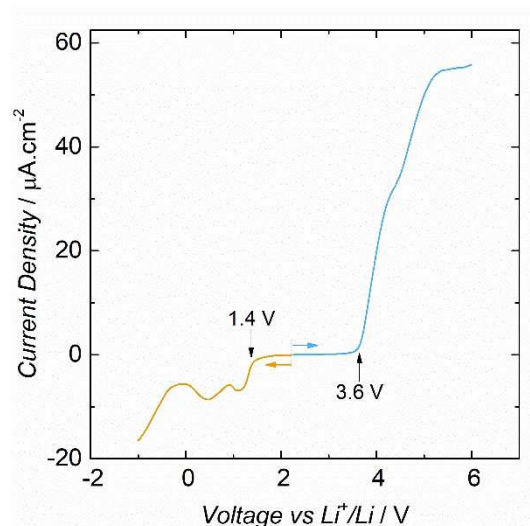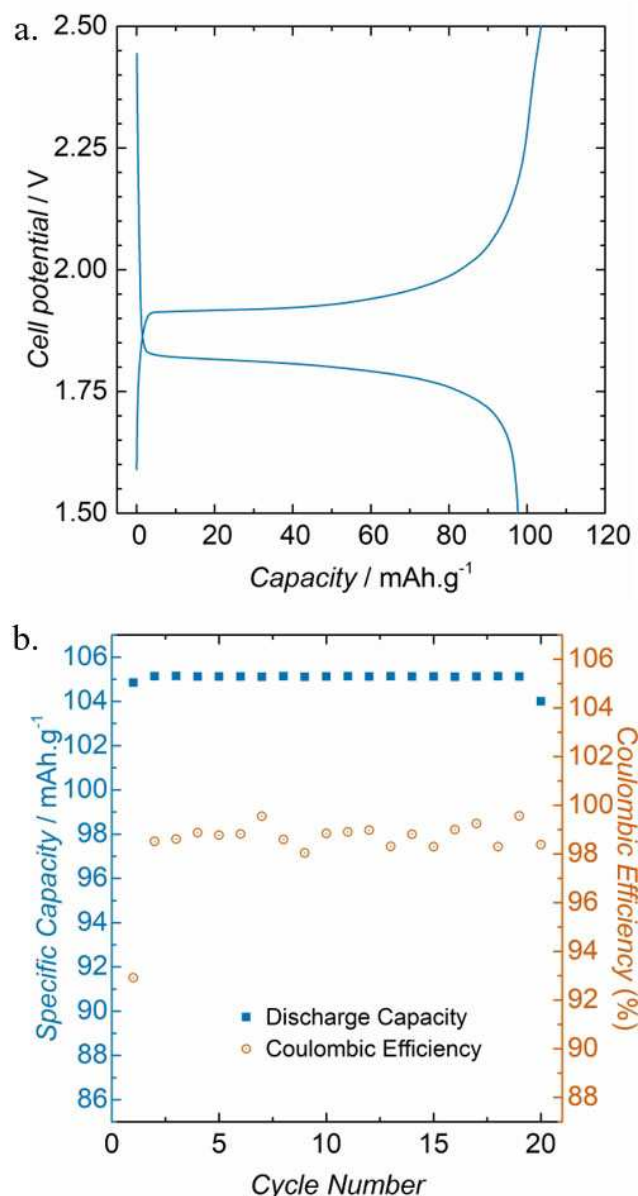WE surface.[35] Overall the SA:MBC 2:1 composite displays an ESW wide enough to be used as a SSE.

Armed with the ion conductivity data and the ESW, as well as the physico-chemical data, the SA:MBC 2:1 composite was investigated in a LTO/SSE/LFP cell at RT, 50, and 70 °C. At RT and 70 °C there were no plateaus found by the galvanostatic cycling and the capacities were lower than expected (Figure S6). We speculate that at RT this is due to the low ion conductivity (3.8×10^{-4} S cm^{-1}), while at 70 °C the ion conducting paths in the SSE might be destroyed. Turning to the cycling at 50 °C, the initial charge/discharge profile of the cell (Figure 6a) shows a plateau at 1.9 V during charge, which corresponds to Li insertion into LTO, while during discharge the plateau, now at 1.8 V, reflects Li extraction. The proof-of-concept cell delivered a specific capacity of ~105 mAh g^{-1} and was reasonably stable for 20 cycles (Figure 6b). While the capacity is 32% lower than the nominal 150 mAh g^{-1} for the LFP used, this can be improved upon by introducing SA:MBC 2:1 into the electrode formulation, hence forming a conduction path also within the electrode particle network,[36] extra important for SSEs, and by reduce the interfacial resistance, crucial for most SSEs.[4] Here, the initial coulombic efficiency was 93%, but it improved to ~99% after the second cycle – and further pre-cycling and conditioning might improve this even further.

3. Conclusions

The novel composite synthesized, consisting of a MBC and a SA shows high conductivity caused by the SA dissociating ~38% of the Li salt, and the MBC providing the lithium ions with conduction paths. The SA:MBC 2:1 composite showed thermal stability over 70 °C, where it melted without subsequent crystallization, but a glass transition at −16 °C. Its ESW of about 3.7 V allowed its testing as electrolyte in a LTO/LFP battery,

99.8%), hexane (95%), tetrahydrofuran (THF,≥99.9%) were all purchased from Sigma Aldrich and used without further purification. LiTFSI (99%) was bought from Solvionic and dried under vacuum for 48 h.

Synthesis of the Silatranes (SA)[12]

TEOS (2.23 ml, 10 mmol) and TEOA (1.33 ml, 10 mmol) were mixed in p-xylene with a catalytic quantity of KOH under magnetic stirring and nitrogen atmosphere in a round bottom flask connected to a distillation column. The axial substituents of the SA were varied by adding 10 mmol of the corresponding hydroxyl containing compound *i.e.* isopropyl alcohol, cyclohexanol, phenol, benzyl alcohol. For ethoxysilatrane, no extra alcohol was added (Scheme 1). The
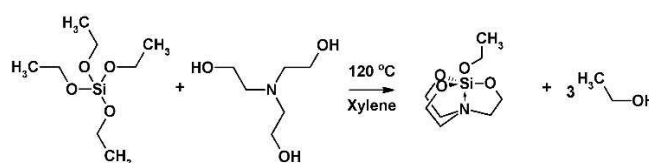
Scheme 1. Reaction scheme for the synthesis of ethoxysilatrane.

solution was allowed to react for 16 h at 120 °C. Ethanol generated in the reaction was continuously transferred from the reactor by distillation and the product was precipitated using hexane (300 ml). The obtained white solid was purified by extraction using hot hexane and recrystallization. The resulting white needles were dried in a vacuum Büchi oven for 14 h at 80 °C and subsequently transferred under vacuum to an argon-filled glove box ($H_2O <$ 1 ppm, $O_2 < 1$ ppm).

As SAs do not present any intrinsic ion conductivity, LiTFSI/SA complexes were prepared by dissolving the SAs in THF, adding 25 mol% of LiTFSI and mixing the solution for homogeneity, and subsequently removing the THF in a vacuum Büchi oven for 2 days at room temperature.

Synthesis of Molecule-Based Crystals (MBC)[13,37]

LiTFSI (287 mg, 1 mmol) and TMEDA (116 mg, 1 mmol) were dissolved in toluene under argon atmosphere and vigorous stirring for 2 h at 80 °C until a colourless homogeneous solution was achieved (Scheme 2). The crystallization proceeded gradually over
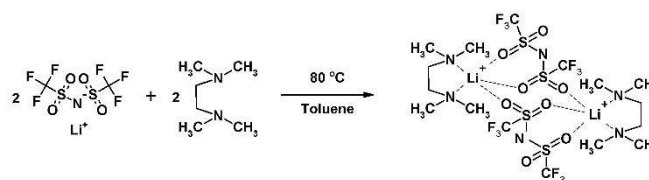
Scheme 2. Reaction scheme for the synthesis of the molecule-based crystal.

three weeks. The white crystals were washed with dry pentane and dried in a vacuum Büchi oven for 3 days at room temperature.

Figure 6. (a) Initial charge/discharge curve and (b) cycle performance of the all-solid-state rechargeable lithium ion cell LTO/SA:MBC 2:1/LFP at 50 °C.

showing capacities up to 105 mAh g^{-1}. Further studies on the ratio of the single components and their interactions might lead to the creation of co-crystals, which could potentially lead to higher conductivity and thermal stability.

Experimental Section

Materials

Tetraethyl orthosilicate (TEOS, 98%), triethanolamine (TEOA, ≥99.0%), potassium hydroxide (KOH,≥85.0%), isopropyl alcohol (≥ 99.0%), cyclohexanol (99%), phenol (≥ 99.5%), benzyl alcohol (99.8%), xylene (≥ 98.5% xylenes + ethylbenzene basis), tetramethylethylenediamine (TMEDA,≥99.5%), pentane (≥ 99%), toluene (≥

Silatrane:Molecule-Based Crystal (SA:MBC) Composites

The SA was dissolved in anhydrous THF and then homogeneously mixed with the MBC in three different molar ratios SA:MBC – 1:1, 2:1, and 1:2. Composite SSEs were obtained by removing the solvent in a vacuum Büchi oven for 3 days at room temperature. The final water content was determined to be < 5 ppm by Karl-Fischer titration using a Metrohm 381 Coulometer.

Additionally, SA:MBC 2:1 composites with some extra LiTFSI content: 5, 15 and 25 wt%, were made by dissolving the appropriate amounts of SA, MBC and LiTFSI in THF, again mixed homogeneously and dried in a vacuum Büchi oven for 3 days at room temperature.

Ion Conductivity and Transport

A Novocontrol broadband dielectric spectrometer equipped with an Alpha-S high-resolution dielectric analyser was used for all measurements. The sample cell had blocking stainless steel electrodes, an inner diameter of 4 mm and a thickness of 1 mm, both defined by a PTFE spacer. The cell was filled with sample inside the argon glove box and transferred to the instrument without access to the atmosphere. The measurements were performed on both the heating and the cooling ramp. Starting at 0 °C, the sample was heated to 100 °C and then cooled to 0 °C in 10 °C steps, using a 15 min equilibration time before measurement at each temperature. The frequency range was 10^{-2} to 10^7 Hz and a 10 mV AC perturbation was used. The ion conductivities were obtained from the radial frequency corresponding to the peak in the imaginary part of the electrical modulus.

The relationship between temperature (T) and ion conductivity (σ) was fitted using the Vogel-Fulcher-Tammann (VFT) Equation (1):

$$\ln\sigma = \sigma_0 - \frac{B}{T - T_0} \tag{1}$$

where σ_0 (S.cm^{-1}) is the pre-factor often related to charge carrier concentration, while B (K) is an empirical parameter related to the apparent activation energy at a given temperature. T_0 (K), also known as the Vogel temperature, is the temperature at which the configurational entropy becomes zero.[15] By setting T_0 to zero, an Arrhenius fit is achieved rather than a VFT. All fitting was performed by using a Levenberg−Marquardt algorithm in the Origin Lab® software.

Structural Characterization

X-ray diffraction (XRD) was performed using a X'Pert Pro diffractometer (Cu Kα radiation, $\lambda = 0.154184$ nm) equipped with an X'Celerator ultrafast RTMS detector. The angular range was 10–50° (in 2θ).

To study the local structure of the TFSI anion both Fourier transform infrared (FTIR) spectroscopy in attenuated total reflection (ATR) mode and FT-Raman spectroscopy were used. For the former a Bruker Alpha spectrometer equipped with a diamond crystal as refractive element and placed inside an argon-filled glove box was used to record IR spectra consisting of 200 scans each collected at room temperature between 480 and 1600 cm^{-1} using a resolution of 2 cm^{-1}. All spectra are represented as a function of the ATR intensity: I = log$_{10}$ (R$_0$/R), where R$_0$ is the ATR intensity after reflection at the diamond/argon interface and R is the ATR intensity after reflection at the diamond/sample interface. Proper contact between the sample and the diamond crystal was assured by applying pressure with the module piston.

The Raman spectroscopy was performed at room temperature using a Bruker MultiRAM FT-Raman spectrometer, with a nitrogen-cooled germanium detector and a resolution of 2 cm^{-1}. A Nd-YAG (1064 nm) laser was used at an operating power of 200 mW and the Raman spectra were derived from 1000–2000 scans. For a detailed analysis of the region 725–765 cm^{-1}, the spectra of MBC and SA:MBC 2:1 were deconvoluted using pseudo-Voigt functions (Gaussian:Lorentzian = 60:40), following the procedure of Lassègues et al.[30]

Thermal Behaviour

The thermal stability was studied by thermogravimetric analysis (TGA) for samples of ~ 20 mg using a Netzsch TG 209 F1 instrument with a resolution of 0.1 μg under N$_2$ gas atmosphere with a flow of 20 mL min^{-1} and a heating rate of 5 °C min^{-1}. The onset temperatures of the weight losses are defined as the intersection point of the extrapolated baseline and the inflectional tangent.

Melting point and phase transformation temperatures were obtained through differential scanning calorimetry (DSC, TA Instruments Q1000) for samples of ~ 10 mg using sealed aluminium pans. A heating rate of 10 °C min^{-1} was used for SA and MBC, while SA:MBC 2:1 was studied at several rates: 1, 10 and 20 °C min^{-1}. The onset temperatures of the transitions are defined as the intersection of the tangents of the peak with the extrapolated baseline.

Electrochemistry and Battery Tests

The electrochemical stability windows (ESW) were assessed at room temperature by linear sweep voltammetry (LSV) at a scan rate of 1 mV s^{-1} using coin cells with nickel foil as working electrode (WE) and lithium foil as counter (CE) and reference (RE) electrode.

ASSB cells were made using lithium iron phosphate (LFP) as the cathode, SA:MBC 2:1 as the SSE, and lithium titanate (LTO) as the anode. The electrodes were purchased from Custom Cells Itzehoe Gmbh (balanced, 12 mm Ø, 90% active material, specific capacity 150 mAh g^{-1}, #353537011 and #353586011, respectively). The SA:MBC 2:1 was ground using an agate mortar and pestle, whereafter the powder was placed in a 13 mm Ø die and a pressure of 1 ton was applied for 5 min resulting in a disk with a thickness of ~ 100 μm. The LFP and LTO electrodes were then placed on each side of the electrolyte pellet created and a pressure of 1 ton was applied for 5 min, and subsequently coin cells were assembled using the resulting three-layer pellet. All cell preparation was performed inside the argon glove box. The ASSB cell cycling tests were performed at a constant current density of 15 mA g^{-1} (0.1 C) in the voltage range from 1.5 to 2.5 V vs. Li$^+$/Li at room temperature, 50 and 70 °C, using a 580 battery cycler from Scribner Associates Inc. (Southern Pines, NC, USA).

Acknowledgements

Conflict of Interest

The authors declare no conflict of interest.

[1] A. Manthiram, X. Yu, S. Wang, *Nat. Rev. Mater.* **2017**, *2*, 16103.
[2] R. C. Agrawal, G. P. Pandey, *J. Phys. D* **2008**, *41*, 223001.
[3] J. B. Goodenough, P. Singh, *J. Electrochem. Soc.* **2015**, *162*, A2387–A2392.
[4] Z. Wu, Z. Xie, A. Yoshida, Z. Wang, X. Hao, A. Abudula, G. Guan, *Renewable Sustainable Energy Rev.* **2019**, *109*, 367–385.
[5] S. B. Aziz, T. J. Woo, M. F. Z. Kadir, H. M. Ahmed, *J. Sci. Adv. Mater. Devices* **2018**, *3*, 1–17.
[6] M. Moriya, H. Kitaguchi, E. Nishibori, H. Sawa, W. Sakamoto, T. Yogo, *Chem. Eur. J.* **2012**, *18*, 15305–15309.
[7] M. Moriya, D. Kato, W. Sakamoto, T. Yogo, *Chem. Eur. J.* **2013**, *19*, 13554–13560.
[8] M. Moriya, K. Nomura, W. Sakamoto, T. Yogo, *CrystEngComm* **2014**, *16*, 10512–10518.
[9] M. Moriya, *Sci. Technol. Adv. Mater.* **2017**, *18*, 634–643.
[10] T. Mizumo, R. Fujita, H. Ohno, J. Ohshita, *Chem. Lett.* **2011**, *40*, 798–800.
[11] T. Mizumo, M. Nakashima, J. Ohshita, *Silicon* **2017**, *9*, 85–96.
[12] J. K. Puri, R. Singh, V. K. Chahal, *Chem. Soc. Rev.* **2011**, *40*, 1791–1840.
[13] M. Moriya, K. Nomura, W. Sakamoto, T. Yogo, *CrystEngComm* **2014**, *16*, 10512–10518.
[14] D. M. Seo, P. D. Boyle, R. D. Sommer, J. S. Daubert, O. Borodin, W. A. Henderson, *J. Phys. Chem. B* **2014**, *118*, 13601–13608.
[15] K. M. Diederichsen, H. G. Buss, B. D. McCloskey, *Macromolecules* **2017**, *50*, 3831–3840.
[16] H. Kageyama, K. Hayashi, K. Maeda, J. M. Rondinelli, K. R. Poeppelmeier, *J. P. Att*, **2018**, DOI 10.1038/s41467-018-02838-4.
[17] D. Wohlmuth, V. Epp, P. Bottke, I. Hanzu, B. Bitschnau, I. Letofsky-Papst, M. Kriechbaum, H. Amenitsch, F. Hofer, M. Wilkening, *J. Mater. Chem. A* **2014**, *12*, 20295–20306.
[18] M. G. Voronkov, *Pure Appl. Chem.* **1966**, *13*, 35–60.
[19] I. Rey, P. Johansson, J. Lindgren, J. C. Lassègues, J. Grondin, L. Servant, *J. Phys. Chem. A* **2002**, *102*, 3249–3258.
[20] R. A. Sanders, R. Frech, M. A. Khan, *J. Phys. Chem. B* **2003**, *107*, 8310–8315.
[21] S. J. Wen, T. J. Richardson, D. I. Ghantous, K. A. Striebel, P. N. Ross, E. J. Cairns, *J. Electroanal. Chem.* **1996**, *408*, 113–118.
[22] M. S. Gaafar, S. Y. Marzouk, *Phys. B* **2007**, *388*, 294–302.
[23] R. Arnaud, D. Benrabah, J.-Y. Sanchez, *J. Phys. Chem.* **2002**, *100*, 10882–10891.
[24] A. Bakker, S. Gejji, J. Lindgren, K. Hermansson, M. M. Probst, *Polymer* **1995**, *36*, 4371–4378.
[25] A. Bakker, J. Lindgren, K. Hermansson, *Polymer* **1996**, *37*, 1871–1878.
[26] J. C. Lassègues, J. Grondin, D. Talaga, *Phys. Chem. Chem. Phys.* **2006**, 5629–5632.
[27] A. Lahiri, T. J. S. Schubert, B. Iliev, F. Endres, *Phys. Chem. Chem. Phys.* **2015**, *17*, 11161–11164.
[28] M. Kerner, N. Plylahan, J. Scheers, P. Johansson, *Phys. Chem. Chem. Phys.* **2015**, *17*, 19569–19581.
[29] S. Duluard, J. Grondin, J.-L. Bruneel, I. Pianet, A. Grélard, G. Campet, M.-H. Delville, J.-C. Lassègues, *J. Raman Spectrosc.* **2008**, *39*, 627–632.
[30] J. C. Lassègues, J. Grondin, C. Aupetit, P. Johansson, *J. Phys. Chem. A* **2009**, *113*, 305–314.
[31] M. Herstedt, M. Smirnov, P. Johansson, M. Chami, J. Grondin, L. Servant, J. C. Lassègues, *J. Raman Spectrosc.* **2005**, *36*, 762–770.
[32] E. H. Lee, S. R. Byrn, *J. Pharm. Sci.* **2010**, *99*, 4013–4022.
[33] F. Kremer, A. Schönhals, Eds., *Broadband Dielectric Spectroscopy*, Springer-Verlag Berlin Heidelberg GmbH, **2003**.
[34] J. Qian, W. A. Henderson, W. Xu, P. Bhattacharya, M. Engelhard, O. Borodin, J. G. Zhang, *Nat. Commun.* **2015**, *6*, DOI 10.1038/ncomms7362.
[35] V. Sharova, A. Moretti, T. Diemant, A. Varzi, R. J. Behm, S. Passerini, *J. Power Sources* **2018**, *375*, 43–52.
[36] A. Sakuda, A. Hayashi, M. Tatsumisago, *Sci. Rep.* **2013**, *3*, 2–6.
[37] M. G. Davidson, P. R. Raithby, A. L. Johnson, P. D. Bolton, *Eur. J. Inorg. Chem.* **2003**, 3445–3452.